

## In-droplet microparticle separation using travelling surface acoustic wave

Kwangseok Park, Jinsoo Park, Jin Ho Jung, Ghulam Destgeer, Husnain Ahmed, and Hyung Jin Sung<sup>a)</sup>

*Department of Mechanical Engineering, Korea Advanced Institute of Science and Technology (KAIST), 291 Daehak-ro, Yuseong-gu, Daejeon 34141, South Korea*

(Received 24 October 2017; accepted 11 December 2017; published online 21 December 2017)

Droplets in microfluidic systems can contain microscale objects such as cells and microparticles. The control of the positions of microscale objects within a microchannel is crucial for practical applications in not only continuous-flow-based but also droplet-based systems. This paper proposes an active method for the separation of microparticles inside moving droplets which uses travelling surface acoustic waves (TSAWs). We demonstrate the preconcentration and separation of 5 and 10  $\mu\text{m}$  polystyrene microparticles in moving water-in-oil droplets through the application of TSAWs with two different frequencies. The microparticles inside the droplets are affected by the acoustic radiation force induced by the TSAWs to move laterally in the direction of the TSAW propagation and are thereby separated according to their size. In-droplet separation is then demonstrated through droplet splitting at a Y-junction. Compared to our previous studies, this acoustic approach offers the label-free and on-demand separation of different-sized micro-objects in moving droplets. The present method has potential uses such as in-droplet sample purification and enrichment. *Published by AIP Publishing.*

<https://doi.org/10.1063/1.5010219>

### I. INTRODUCTION

Droplet microfluidics has been widely utilized in various applications including biochemical analysis<sup>1</sup> and medical diagnosis.<sup>2</sup> Two immiscible phases form compartmentalized droplets, so each droplet can serve as an individual and isolated microreactor.<sup>3</sup> The reaction time and the consumption of reagents and samples can be reduced because the volume of single droplet in a microchannel is typically in the picoliter to nanoliter range. Droplets encapsulating microscale objects (e.g., cells and microparticles) can currently be prepared at high production rates up to tens of kHz.<sup>4</sup> Droplets are also useful for performing biochemical reactions associated with intracellular conditions or for mimicking cells.<sup>5,6</sup> Several useful protocols, such as the sorting of droplets<sup>7–11</sup> containing target contents and the merging of droplets<sup>12–15</sup> to add new reagents, have been reported. Since these operations have potential uses in precise analyses and assays, droplet-based microfluidic systems have been adopted in a number of applications such as material synthesis,<sup>16,17</sup> polymer chain reaction (PCR),<sup>18,19</sup> cell incubation,<sup>20</sup> and drug screening.<sup>21</sup> In particular, it is advantageous to use droplet-based microfluidic systems to handle a small number of microparticles or cells.<sup>1</sup> The measurement of the microenvironments in droplets can be performed singly or at the level of small groups, whereas analyses inside continuous-flow-based systems are performed at the population level due to advective and diffusive mixing.<sup>22</sup>

In-droplet separation is of great importance when dealing with droplets that contain different-sized contents. If non-target impurities are separated from the sample, the detection signal can be significantly improved due to the decreased background noise.<sup>23</sup> The in-droplet separation can be utilized for the purification and enrichment of individual target samples in a mixture.<sup>24</sup> Micro-

---

<sup>a)</sup> Author to whom correspondence should be addressed: [hjsung@kaist.ac.kr](mailto:hjsung@kaist.ac.kr)

object separation can be achieved in either continuous flows or droplets. The control of the positions of microscale objects is of paramount importance in both continuous-flow-based and droplet-based systems although continuous-flow-based microfluidic systems are usually selected for separation processes.<sup>25–28</sup> Separating the sample mixture first in the continuous flow mode and then encapsulating it into the droplet are an alternative to in-droplet separation. However, the system for this alternative approach must integrate both modes, which is likely to enlarge the system scale because the number of inlets and outlets will rise, which can increase the complexity of the system. Despite the advantage and potential of in-droplet separation, significant aspects of in-droplet separation remain under-explored because its mechanism is inherently complex: internal vortices are present inside the droplet and its flow conditions are multiphase.<sup>29</sup>

In contrast to the vibrant research advances in continuous-flow-based microfluidic microparticle separation, a few in-droplet separation methods have been proposed. Hein *et al.* induced the accumulation of microparticles at the rear of droplets by using hydrodynamic precipitation.<sup>30</sup> Wang *et al.* used posts inside a microchannel to capture beads in droplets.<sup>31</sup> Although these passive methods are simple since they do not require external forces, they are not capable of the on-demand control of the positions of microscale objects. Furthermore, precipitation requires a long process time; in addition, the particles filtered out of the droplet are temporarily exposed to the continuous flow before recapture. In order to reduce the time consumed and enable on-demand manipulation, active methods for the separation of microparticles with external forces, such as electric,<sup>32,33</sup> magnetic,<sup>23,34,35</sup> and acoustic forces,<sup>27,35–37</sup> have been proposed. For the active in-droplet manipulation, locally intense external forces can enable the fine control of interior microparticles. Electric and magnetic methods utilize long-range interactions and so are probably not suitable for in-droplet manipulation. In addition, such separation processes require particles with magnetic properties or electric polarity. Unlike other active methods, the acoustic method offers label-free separation based on mechanical properties (e.g., density, size, and compressibility).<sup>37</sup> Recently, Fornell *et al.* demonstrated the control of the lateral positions of microscale objects inside droplets by using the first<sup>24</sup> and second<sup>36</sup> harmonic modes of standing bulk acoustic waves (SBAWs). Ohlin *et al.* proposed a method for the two-dimensional manipulation of particles in droplets using the half-wave resonances of two BAWs from dual transducers.<sup>38</sup> However, these acoustic methods are limited to the in-droplet microparticle preconcentration of single species.

None of the reported methods has accomplished the in-droplet separation of different-sized micro-objects. Here, we propose an acoustic method that uses travelling surface acoustic waves (TSAWs) to concentrate and separate particles with two different sizes inside droplets. This study primarily focuses on proving the applicability of the present acoustic method to the in-droplet particle separation. Several studies have reported that TSAWs can be utilized for micro-object control or fluid actuation in droplet-based microfluidic systems.<sup>39–42</sup> The TSAW-based acoustic method has the following advantages over previously reported SBAW-based methods: (1) the tuning of frequencies over a wider and higher range;<sup>43</sup> (2) higher energy efficiency due to the confinement of energy to the substrate surface rather than the bulk; (3) the ease of observation in polymer microchannels due to higher optical transparency; (4) polymer microchannels that can be fabricated with soft lithography rather than etching. In this study, polystyrene (PS) particles were suspended in water-in-oil droplets moving along a polydimethylsiloxane (PDMS) microchannel. The acoustic radiation forces (ARFs) induced by the two TSAWs affect the PS particles with different sizes differently; as a result, they take up different positions, thereby realizing separation inside the droplet. The mother droplet can then be split into two daughter droplets containing particles of different sizes. Our TSAW-based method realizes the in-droplet separation of microparticles of two different sizes. Therefore, the proposed acoustic method can serve as an in-droplet sample purification and enrichment tool in droplet-based microfluidic systems.

## II. RESULTS AND DISCUSSION

### A. Working mechanism

In our study of in-droplet particle preconcentration and separation, we use PS particles with diameters of 5 and 10  $\mu\text{m}$ . The TSAWs are generated by slanted finger interdigital

transducers (SFITs) with electrode spacings that vary linearly. The SFITs have a working frequency bandwidth; as a result, each SFIT enables the generation of TSAWs with different frequencies. The TSAWs propagate along a piezoelectric substrate and refract into the microchannel that the droplets move along. In the fluid domain, the TSAWs are converted into longitudinal waves that apply ARFs to the droplet interface. Inspired by the research of King,<sup>44</sup> several theoretical calculations of the ARF on a sphere have been presented.<sup>45–47</sup> To determine the frequency that enables the effective manipulation of the PS particles, we calculated in our previous study of dependences of the ARF factors on the diameter of the PS particles and the TSAW frequency.<sup>48</sup> The ARF factor ( $F_F$ ) is dimensionless with respect to the acoustic energy density and the cross-sectional area of the particle (see [supplementary material](#) for details). The results of our theoretical calculations shown in Fig. 1 indicate that a frequency of approximately 135 MHz is required to control both particles and a frequency of approximately 100 MHz is required to manipulate the 10  $\mu\text{m}$  PS particles. These estimations cannot be directly matched to frequencies used in the experiments since these determinations of the ARFs on particles assumed an unbound surrounding medium (i.e., a continuous-fluid-based system). We investigated whether the particles were pushed in the direction of the TSAW propagation when exposed to TSAWs at different frequencies based on our theoretical estimation. The results are given in Table I. Based on these results, 135 MHz and 95 MHz were used in the experimental demonstrations to control the particles of both sizes and 10  $\mu\text{m}$ , respectively.

A schematic diagram of the TSAW-based method for particle manipulation inside droplets is shown in Fig. 2(a). At the interface between the substrate and the fluid inside the microchannel, TSAWs refract into the fluid domain at a Rayleigh angle  $\theta_r$ . Since the wavelengths of 95 MHz TSAWs in water and oil (15.6 and 6.8  $\mu\text{m}$ , respectively) are smaller than the scale of the droplets, we can use a ray acoustic approach.<sup>39,49</sup> The interface of the fluids is assumed to be flat by the thin oil film between the droplets and the channel walls. The effect of the thin film could be negligible for the following reasons. First, the curvature of the droplet in the  $y$ - $z$  plane is relatively small compared to the channel width [see Fig. 2(b)]. Second, the acoustic wave attenuation lengths are longer than the channel width. The acoustic wave attenuation length on the substrate surface ( $x_s$ ) is defined as  $x_s = \rho_p c_s \lambda_s / \rho_f c_f$ , where  $\rho_s$  and  $\rho_f$  are the density of the substrate and the fluid;  $c_s$  and  $c_f$  are the sound speed on the substrate and in the fluid, and  $\lambda_s$  is the SAW wavelength on the substrate surface, respectively.<sup>41</sup> The attenuation lengths of 96 and 135 MHz TSAWs were calculated as 525 and 370  $\mu\text{m}$ , respectively, while the channel width was 200  $\mu\text{m}$ . Third, the presence of the thin film did not significantly reduce power transmission. For the incidence of the acoustic

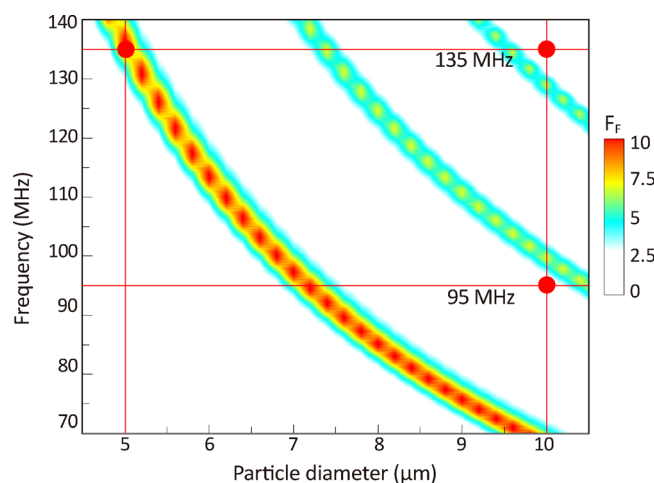


FIG. 1. The variations in the acoustic radiation force factor ( $F_F$ ) with the PS particle size and the TSAW frequency for a continuous-flow-based microfluidic system. The optimal TSAW frequencies for the control of 5 and 10  $\mu\text{m}$  PS particles in a droplet can be estimated from these results. The frequencies used for in-droplet manipulation (three red dots) are slightly different from the estimates because of the differences between the theoretical and experimental systems.

TABLE I. Results of the in-droplet particle manipulation tests. The symbols in the table were marked depending on percentage of the manipulated particles through image processing using ImageJ (O for more than 70% and X for less than 70%).

$d_p$ ( $\mu\text{m}$ )	$f$ (MHz)						
	80	85	90	95	125	130	135
5	X	X	X	X	O	O	O
10	O	O	O	O	O	O	O

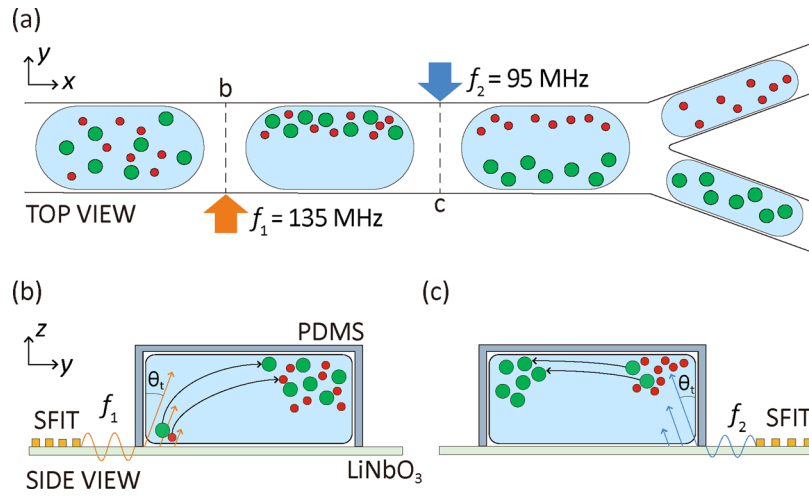


FIG. 2. (a) A top view schematic diagram of the acoustomicrofluidic in-droplet separation system. The 135 MHz TSAWs affect both sizes and the 95 MHz TSAWs affect the larger particles only, so the lateral positions of the 5 and 10  $\mu\text{m}$  PS particles can be controlled. After splitting at a Y-junction, in-droplet separation is demonstrated. (b) and (c) Side view schematic diagrams of the ARF actions of the first and second SFITs, respectively.

rays to the flat interface between the water and the oil, the power transmission coefficient  $\Pi_t$  is calculated as 0.96 using

$$\Pi_t = 4 \frac{Z_o}{\cos\theta_o} \frac{Z_w}{\cos\theta_w} \left/ \left( \frac{Z_o}{\cos\theta_o} + \frac{Z_w}{\cos\theta_w} \right)^2 \right., \quad (1)$$

where  $Z_o$  and  $Z_w$  are the characteristic acoustic impedances of the oil and the water, and the angles  $\theta_o$  and  $\theta_w$  hold the following relation  $c_s = c_o/\sin\theta_o = c_w/\sin\theta_w$  (see [supplementary material](#) for the derivation of the power transmission coefficient). This implies that the power transmission due to refraction overwhelms the reflection on the interface despite the change of acoustic impedances. The refraction angle can be estimated as  $22^\circ$  according to Snell's law by using the speeds of sound inside the water and the substrate.

The effects of the acoustic streaming flow can be neglected since the Helmholtz number of particles ( $\kappa = \pi d_p f / c_f$ ) is greater than 1.<sup>50</sup> As plug-type droplets are fitted to the channel inner-walls, the droplet movement in the direction of the wave propagation is restricted. The micro-particles within the droplet are randomly distributed initially but are then translocated by the ARF depending on the particle size and the TSAW frequency. For in-droplet particle separation, the 135 MHz ( $f_1$ ) and 95 MHz TSAWs ( $f_2$ ) are employed for both particle types [Fig. 2(b)] and the 10  $\mu\text{m}$  particles [Fig. 2(c)], respectively. When exposed to the  $f_1$  TSAWs, both particles are pushed in the wave propagating direction. On the other hand, the  $f_2$  TSAWs propagate in the opposite direction to the  $f_1$  TSAWs and affect only the 10  $\mu\text{m}$  PS particles. Once the lateral positions of the 10  $\mu\text{m}$  particles are differentiated from those of the 5  $\mu\text{m}$  particles, the droplet

is split into two daughter droplets at a downstream Y-junction. Finally, the size of the particles in each daughter droplet is different, and thus, the in-droplet separation is achieved.

## B. In-droplet preconcentration

As a prerequisite for in-droplet particle separation, the preconcentration of microparticles within droplets was demonstrated in our device, as shown in Fig. 3. A SFIT with a working frequency range of 105–145 MHz was used to manipulate both types of microparticles (5 and 10  $\mu\text{m}$ ) according to Table I (see the movie in the [supplementary material](#)). The volumetric flow rate was 130  $\mu\text{l/h}$ , and the droplet velocity was 3.3 mm/s. In the absence of the acoustic field, the particles move along inner vortices inside the moving droplet; the streamlines inside the droplet have closed shapes and are symmetrical with respect to the center line of the droplet, as depicted in Fig. 3(a). The microparticles located near the channel walls move in the same direction as the droplet motion while those located near the center line of the microchannel move in the opposite direction. Figure 3 presents microscopic snapshots of the in-droplet preconcentration of the 5 and 10  $\mu\text{m}$  microparticles through the application of the 135 MHz TSAWs ( $0.63 V_{\text{rms}}$ ). In the droplet, the lateral positions of both types of PS particles are controlled in the direction of TSAW propagation. When exposed to the TSAWs, the microparticles circulating along the lower inner vortex deviate from their original streamlines and are thus translocated to the upper vortex. The droplet is split into two daughter droplets with the same volume at the downstream Y-junction. One of these daughter droplets has a much higher population of particles than the other, resulting in an in-droplet particle preconcentration. Although a majority of the PS particles was effectively manipulated by the ARF of the TSAWs, a few particles near the channel walls did not move to the desired lateral position and hence resided in the daughter droplet containing fewer particles (see the movie in the [supplementary material](#)). The in-droplet preconcentration can be limited due to internal vortices and anechoic zones, as discussed below.

## C. In-droplet separation

In-droplet microparticle separation was realized by selectively separating the 10  $\mu\text{m}$  PS particles from the preconcentrated particles by using 95 MHz TSAWs radiating from the second SFIT. The flow rate and the droplet velocity were the same as those used for the in-droplet preconcentration. As discussed in Sec. II A, the ARF of 95 MHz TSAWs acting on the 5  $\mu\text{m}$  PS particles is not strong enough to translocate them. Therefore, the two types of particles with different sizes take up distinct and lateral positions, as shown in Fig. 4. For the second SFIT, we

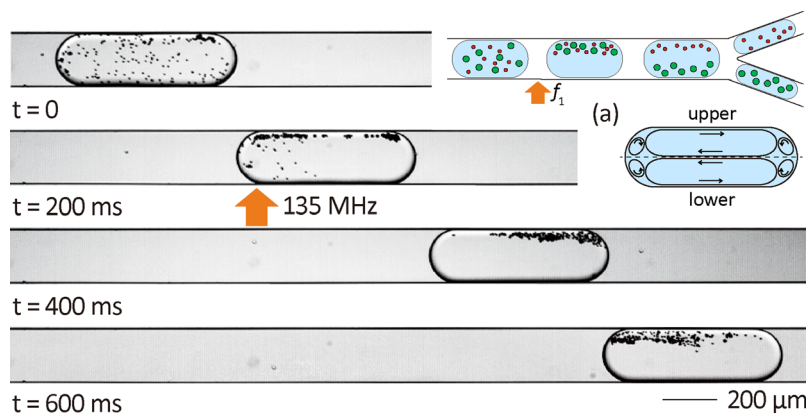


FIG. 3. Images of the experimental in-droplet preconcentration. The PS particles in the droplets are manipulated to be pushed in the direction of TSAW propagation. Before the ARF action, the particles circulate in the moving droplet. However, the ARF due to the 135 MHz TSAWs ( $0.63 V_{\text{rms}}$ ) moves both the 5 and 10  $\mu\text{m}$  particles to the streamline in the upper zone. The particles become concentrated in the droplet within 400 ms. The volumetric flow rate was 130  $\mu\text{l/h}$ , and the droplet velocity was 3.3 mm/s.



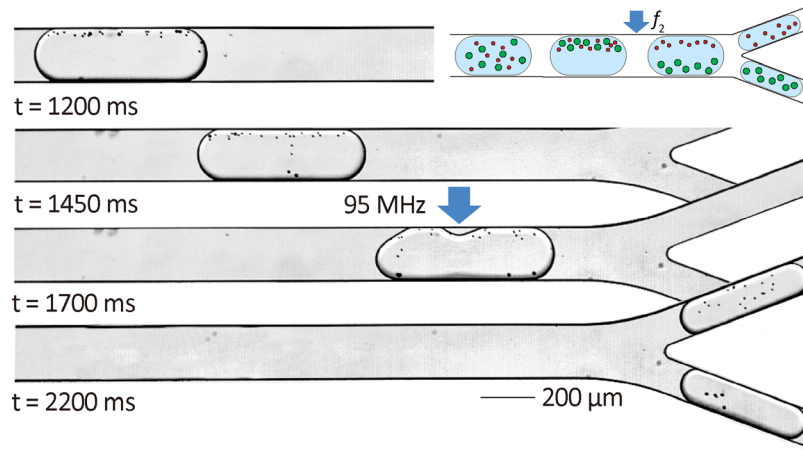


FIG. 4. Images of experimental in-droplet separation. After the PS particles are concentrated by the first 135 MHz TSAWs, the 95 MHz TSAWs are applied in the opposite direction to that of the 135 MHz TSAWs, which moves the 10  $\mu\text{m}$  PS particles to lower streamlines. In the moving droplet, the 10  $\mu\text{m}$  PS particles have lateral positions distinct from those of the 5  $\mu\text{m}$  particles. The droplet bifurcates downstream and the in-droplet separation is demonstrated: the daughter droplets contain PS particles with different sizes. The flow rate and the droplet velocity are the same as those in Fig. 3.

used a SFIT with a frequency bandwidth of 75–95 MHz; the first SFIT was the same as the SFIT used for the in-droplet preconcentration. After the ARF of 135 MHz TSAWs pushed both types of PS microparticles into the corresponding propagation direction, the larger particles were moved by the 95 MHz TSAWs ( $0.707 V_{\text{rms}}$ ) produced from the second SFIT in the opposite direction to that of the first TSAWs. The 10  $\mu\text{m}$  particles on the upper streamlines were moved to the lower streamlines in the droplet. The droplet was then split into two daughter droplets at the downstream Y-junction. The particles with different sizes were separated; the daughter droplets at the upper and lower sides contained 5 and 10  $\mu\text{m}$  particles, respectively.

For quantitative assessment, the efficiencies of the separation of the 5  $\mu\text{m}$  ( $\eta_{s5}$ ) and 10  $\mu\text{m}$  ( $\eta_{s10}$ ) particles were defined as

$$\eta_{s5} = \frac{n_{u5}}{n_{u5} + n_{l5}}, \quad \eta_{s10} = \frac{n_{l10}}{n_{u10} + n_{l10}}, \quad (2)$$

where  $n_{u5}$  and  $n_{u10}$  are the numbers of 5 and 10  $\mu\text{m}$  particles, respectively, in the upper daughter droplet, and  $n_{l5}$  and  $n_{l10}$  are the numbers of 5 and 10  $\mu\text{m}$  particles, respectively, in the lower daughter droplet. In the experiments, the in-droplet separation efficiencies of the 5 and 10  $\mu\text{m}$  particles were calculated as  $86.3 \pm 3.3\%$  and  $86.9 \pm 6.0\%$ , respectively. The separation inside the droplet depends on the ARF of the second TSAWs. As the in-droplet method is a size-based kinetic separation, an increase in the ARF magnitude does not guarantee that the movement of the 5  $\mu\text{m}$  particles will be negligible. To examine the variation in the efficiency with the ARF, we altered the ARF of the second TSAW by changing the applied voltage. Figure 5(a) shows the variations with the voltage applied to produce the second TSAWs in the in-droplet separation efficiency of each particle type. For the 10  $\mu\text{m}$  PS particles, the separation efficiency is  $68.5 \pm 6.2\%$  at  $0.398 V_{\text{rms}}$  and increases up to  $91.4 \pm 4.2\%$  at  $0.793 V_{\text{rms}}$ . On the other hand, the efficiency of the 5  $\mu\text{m}$  decreases as the applied voltage increases, reaching  $81.1 \pm 2.8\%$  at  $0.793 V_{\text{rms}}$  even though the separation efficiency is very high for the range  $0.398$ – $0.562 V_{\text{rms}}$ , more than 90%. The increase in the separation efficiency of the 10  $\mu\text{m}$  particles with the increase in the applied voltage can be explained as follows. First, the ARF on the 10  $\mu\text{m}$  particles inside the droplet increases with the increase in the applied voltage. Second, small deformations of the droplet boundaries also move the particles. However, for applied voltages above  $0.562 V_{\text{rms}}$ , boundary deformation can result in movement of the 5  $\mu\text{m}$  particles to the lower zone in the droplet, so the separation efficiency of the 5  $\mu\text{m}$  particles is reduced in contrast to that of the 10  $\mu\text{m}$  particles. The applied voltage should be optimized, not maximized, to enhance the

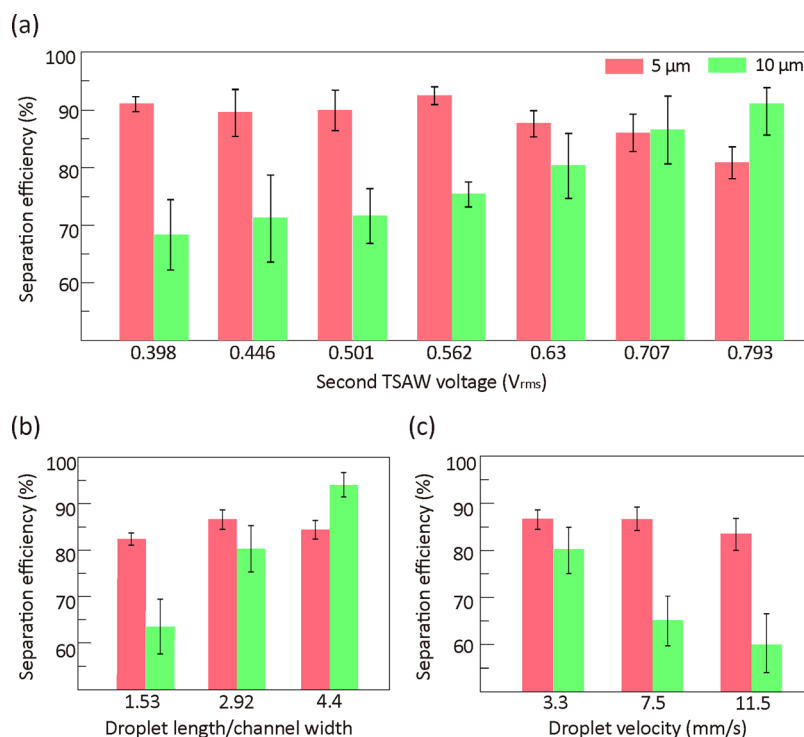


FIG. 5. (a) The variation in the in-droplet separation efficiencies with the voltage applied to produce the second TSAWs. The total flow rate and the droplet velocity are the same as those in Fig. 3. (b) The variation in the in-droplet separation efficiencies with the ratio of the droplet length to the channel width. The flow rates of the water and oil phases were controlled to vary the droplet size while maintaining the constant total flow rate. (c) The variation in the in-droplet separation efficiencies with the droplet velocity. The flow rates of the water and oil phases were controlled to vary the droplet velocity while maintaining the flow rate ratio for the constant droplet size. The applied voltage for the second TSAW in (b) and (c) was  $0.63 V_{rms}$ . Error bars are marked as one standard deviation.

in-droplet separation efficiency. We also conducted experiments by varying the droplet size and the droplet velocity to see the effects of these parameters on the separation efficiency, as shown in Figs. 5(b) and 5(c). With fixed applied voltages of  $0.707$  and  $0.63 V_{rms}$  for the first and second SFITs, respectively, we altered the flow conditions to vary the droplet size and the droplet velocity. In both sets of experiments, the separation efficiency of the  $5 \mu\text{m}$  particles did not show a significant difference from the average value of approximately 85% while that of the  $10 \mu\text{m}$  particles varied significantly regarding the flow conditions. This was because the magnitude of the ARF acting on the  $5 \mu\text{m}$  particles was greater than that of the  $10 \mu\text{m}$  particles, as shown in Fig. 1. Figure 5(b) shows the separation efficiency with respect to the ratio of the droplet length to the channel width. The droplet size was varied by increasing the ratio from 1.53 to 4.4 while maintaining the total flow rate. The separation efficiency of  $10 \mu\text{m}$  increased with the ratio; the efficiency was  $63.1 \pm 7.3\%$  at the ratio of 1.53 and reached  $93.5 \pm 3.2\%$  at the ratio of 4.4. Figure 5(c) shows the separation efficiency with respect to the droplet velocity. The droplet velocity was increased from 3.3 to 11.5 mm/s while maintaining the droplet size. With increasing the droplet velocity from 3.3 to 11.5 mm/s, the separation efficiencies of both 5 and  $10 \mu\text{m}$  decreased from  $88 \pm 2.4\%$  to  $83.5 \pm 3.4\%$  and from  $80.6 \pm 5.7\%$  to  $60.1 \pm 7.7\%$ , respectively. This was attributed to the fact that the increased droplet velocity impeded the particles within the droplet to be exposed to the acoustic field for a sufficient period of time. From the results, we found that increasing the droplet length (i.e., droplet size) and decreasing the droplet velocity allow the microparticles to be exposed to the ARF for a sufficient period of time, leading to an increase in the separation efficiency.

A few intrinsic factors interfere with the in-droplet manipulation of microparticles: anechoic spaces and internal vortices. Anechoic spaces where the particles inside the droplets are only

weakly affected by acoustic waves are present in microchannels in continuous-flow-based microsystems.<sup>48</sup> Anechoic zones are also likely to be present in our droplet-based microfluidic system. The side view of the microchannel in our system can be understood as a continuous-flow-based system because the droplets have a pancake shape that fits the microchannel with an approximate ratio of the height to width of 1:4.35 (i.e., there is less curvature in the height direction). In the case of lateral rightward [Fig. 2(b)] and leftward [Fig. 2(c)] wave propagation, the top-left corner and the top-right corner of the droplet (or the microchannel) in the side view are anechoic spaces. The ARF is very weak in these corner regions, so PS particles located there cannot be manipulated.

In addition, the flow patterns inside the droplet can also be an obstacle to separation. As the droplet moves along the microchannel, the relative velocity field inside the droplet contains three pairs of vortices that are symmetrical with respect to the center line of the microchannel [Fig. 3(a)].<sup>29,51</sup> The particles inside the droplet circulate in the main vortex. Additional small vortices are present at the front and rear of the droplet. The interface deformation resulting from the ARF induced by the TSAWs means that the relative velocity field is no longer symmetric, but these vortices will still be present. In spite of the effects of the ARF and droplet deformation on the lateral positions of the microparticles, a few 10  $\mu\text{m}$  particles become trapped in the small vortex and cannot escape (see the movie in the [supplementary material](#)). Acoustic in-droplet separation with 100% efficiency is difficult for the abovementioned inherent reasons. Nevertheless, our results do provide the first demonstration of the use of acoustics to perform size-based in-droplet microparticle separation at a relatively high efficiency. The heating by the TSAWs in our system was negligible during the in-droplet particle manipulation. We placed a PDMS membrane on the SFIT to measure the temperature increase (see the IR images in the [supplementary material](#)). The temperature increase of the PDMS membrane caused by the 135 MHz TSAW at 0.63  $V_{\text{rms}}$  was less than 1.5 °C, where the applied voltage conditions for our experiments were less than 1  $V_{\text{rms}}$ .

### III. MATERIALS AND METHODS

The device was fabricated by attaching a PDMS microchannel to a piezoelectric substrate with two SFITs consisting of patterned metal electrodes. The microchannel mold was fashioned with SU-8 (SU-8 2050, MicroChem, USA) by using soft lithography. A mixture of the PDMS base and curing agent in a mass ratio of 10:1 was poured into the mold and cured in an oven at 95 °C for 1 h. After curing, the PDMS microchannel was prepared for bonding to the device by cutting it into the desired shapes and punching holes for the inlets and outlets. The height of the PDMS microchannel is 46  $\mu\text{m}$ , and the width is 200  $\mu\text{m}$ . The substrate and the PDMS microchannel were treated with oxygen plasma, and the plasma-treated surface of the PDMS microchannel was bonded to the substrate. The bonded PDMS microchannel was left in the oven at 95 °C for 20 min to enhance the bonding. Additional hydrophobic wall treatment of the PDMS microchannel was performed by injecting a fluorocarbon oil (EGC-1720, 3M, USA) and allowing it to dry. The bimetallic electrodes composed of 30 nm chrome and 100 nm gold were deposited on the lithium niobate piezoelectric substrate (0.5 mm, 128° Y-cut, X-propagating, 2 sp, MTI Korea) by using an e-beam evaporation process. The piezoelectric substrate was covered with an additional 200 nm  $\text{SiO}_2$  layer to improve microchannel bonding and prevent damage to the electrodes. To produce the two TSAWs with frequencies of 135 and 95 MHz, we used two SFITs with linearly varying electrode spacings of 6.5–9  $\mu\text{m}$  and 10–12.5  $\mu\text{m}$ , respectively. The resonant frequency bandwidths of the two SFITs were measured by using a vector network analyzer (TTR503A, Tektronix, USA) and found to be 105–145 MHz and 75–95 MHz, respectively, (the S11 parameters are presented in the [supplementary material](#)). Their finger pair was 40, and their total aperture was 1 mm. Two signal generators (N5171B and N5181A, Keysight, USA) were used to produce electric AC signals with frequencies matching the two resonant frequencies of the SFITs. The signals were amplified through two signal amplifiers (LZY-22+ and ZHL-100 W-GAN+, Mini Circuits, USA), and each SFIT of the device was wired so as to be connected to the amplifier.



For in-droplet preconcentration and separation of microscale objects, we used water-in-oil droplets containing 5 and 10  $\mu\text{m}$  PS particles (Duke Standards<sup>TM</sup>, Thermo Scientific, USA). To reduce sedimentation, one of the obstacles to carrying particles in the droplets, we matched the density of the water to the density of the PS particles,  $1.05\text{ g/cm}^3$ , by mixing heavy water (Sigma Aldrich, USA) and deionized water (Sinhan Science Tech, Korea). An engineering oil (HFE-7500, 3M, USA) was selected to encapsulate the dispersed water, and 2 wt. % of surfactant (Pico-Surf<sup>TM</sup>1, Dolomite Microfluidics, UK) was dissolved in the oil to stabilize droplet forming and prevent droplet merging. The oil and the water were injected into the microchannel inlets by using a syringe pump (neMESYS Cetoni GmbH, Germany). Droplets were generated with a pancake shape that fits within the microchannel walls. The flow rates of the oil and the water were 100 and 30  $\mu\text{l/h}$ , respectively; the droplets moved along the channel at a speed of 3.3 mm/s. Images of in-droplet particle manipulation were recorded with a high-speed camera (pco.1200 hs, PCO, Germany) mounted on an inverted microscope (IX71, Olympus, USA). To calculate the in-droplet separation efficiency, the PS particles were counted manually or by using the ImageJ software (<http://rsbweb.nih.gov/ij/index.html>).

#### IV. CONCLUSIONS

We have developed a droplet-based acoustomicrofluidic system using two SFITs for label-free, on-demand in-droplet separation of PS microparticles with two different sizes. When the ARF induced by the TSAWs causes these particles to move in the direction of wave propagation, the particle distribution within the droplet becomes uneven, and the particles are concentrated. For in-droplet separation, the second TSAWs, which only affect the particles of one particular size, were applied to the preconcentrated microparticles to change the lateral position of the target particles selectively. Then, by splitting the droplet containing the PS microparticles, whose lateral positions depend on their diameters, in-droplet separation was demonstrated. We discovered that the ARF induced by the TSAWs should be optimized to achieve high separation efficiency because the ARF also acts on the droplet interface. As the proposed method offers on-demand, size-based in-droplet particle manipulation, it can be utilized for droplet-based sample purification and enrichment.

#### SUPPLEMENTARY MATERIAL

See [supplementary material](#) for the experimental video, the information of S11 parameter of SFITs, the power transmission with the ray acoustic approach at the interface of the water and the oil, the calculation of ARF factor, and the IR camera images.

#### ACKNOWLEDGMENTS

This work was supported by the Creative Research Initiatives (No. 2017-013369) program of the National Research Foundation of Korea, the KUSTAR-KAIST Institute and the Korea Polar Research Institute (KOPRI).

- <sup>1</sup>M. T. Guo, A. Rotem, J. A. Heyman, and D. A. Weitz, *Lab Chip* **12**, 2146 (2012).
- <sup>2</sup>S. K. Arya, B. Lim, and A. R. A. Rahman, *Lab Chip* **13**, 1995 (2013).
- <sup>3</sup>H. Song, D. L. Chen, and R. F. Ismagilov, *Angew. Chem., Int. Ed.* **45**, 7336 (2006).
- <sup>4</sup>P. Zhu and L. Wang, *Lab Chip* **17**, 34 (2017).
- <sup>5</sup>T. S. Kaminski, O. Scheler, and P. Garstecki, *Lab Chip* **16**, 2168 (2016).
- <sup>6</sup>T. Schneider, J. Kreutz, and D. T. Chiu, *Anal. Chem.* **85**, 3476 (2013).
- <sup>7</sup>J. Park, J. H. Jung, G. Destgeer, H. Ahmed, K. Park, and H. J. Sung, *Lab Chip* **17**, 1031 (2017).
- <sup>8</sup>E. Kadivar, S. Herminghaus, and M. Brinkmann, *J. Phys.: Condens. Matter* **25**, 285102 (2013).
- <sup>9</sup>L. Mazutis, J. Gilbert, W. L. Ung, D. A. Weitz, A. D. Griffiths, and J. A. Heyman, *Nat. Protoc.* **8**, 870 (2013).
- <sup>10</sup>B. Ahn, K. Lee, R. Panchapakesan, and K. W. Oh, *Biomicrofluidics* **5**, 24113 (2011).
- <sup>11</sup>C. N. Baroud, J. P. Delville, F. Gallaire, and R. Wunenburger, *Phys. Rev. E* **75**, 46302 (2007).
- <sup>12</sup>M. Zagnoni and J. M. Cooper, *Lab Chip* **9**, 2652 (2009).
- <sup>13</sup>L. M. Fidalgo, C. Abell, and W. T. S. Huck, *Lab Chip* **7**, 984 (2007).
- <sup>14</sup>V. B. Varma, A. Ray, Z. M. Wang, Z. P. Wang, and R. V. Ramanujan, *Sci. Rep.* **6**, 37671 (2016).
- <sup>15</sup>I. Akartuna, D. M. Aubrecht, T. E. Kodger, and D. A. Weitz, *Lab Chip* **15**, 1140 (2015).
- <sup>16</sup>W. J. Duncanson, T. Lin, A. R. Abate, S. Seiffert, R. K. Shah, and D. A. Weitz, *Lab Chip* **12**, 2135 (2012).

- <sup>17</sup>T. Nisisako, *Curr. Opin. Colloid Interface Sci.* **25**, 1 (2016).
- <sup>18</sup>R. Yang, A. Paparini, P. Monis, and U. Ryan, *Int. J. Parasitol.* **44**, 1105 (2014).
- <sup>19</sup>C. Koepfli, W. Nguitragool, N. E. Hofmann, L. J. Robinson, M. Ome-Kaius, J. Sattabongkot, I. Felger, and I. Mueller, *Sci. Rep.* **6**, 39183 (2016).
- <sup>20</sup>I. Barbulovic-Nad, S. H. Au, and A. R. Wheeler, *Lab Chip* **10**, 1536 (2010).
- <sup>21</sup>K. Kwapiszewska, A. Michalczuk, M. Rybka, R. Kwapiszewski, and Z. Brzózka, *Lab Chip* **14**, 2096 (2014).
- <sup>22</sup>D. J. Collins, A. Neild, A. deMello, A.-Q. Liu, and Y. Ai, *Lab Chip* **15**, 3439 (2015).
- <sup>23</sup>E. Brouzes, T. Kruse, R. Kimmerling, and H. H. Strey, *Lab Chip* **15**, 908 (2015).
- <sup>24</sup>A. Fornell, J. Nilsson, L. Jonsson, P. K. Periyannan Rajeswari, H. N. Joensson, and M. Tenje, *Anal. Chem.* **87**, 10521 (2015).
- <sup>25</sup>L. R. Huang, *Science* **304**, 987 (2004).
- <sup>26</sup>M. Yamada, M. Nakashima, and M. Seki, *Anal. Chem.* **76**, 5465 (2004).
- <sup>27</sup>P. R. C. Gascoyne and J. Vykoukal, *Electrophoresis* **23**, 1973 (2002).
- <sup>28</sup>F. Petersson, L. Åberg, A. M. Swärd-Nilsson, and T. Laurell, *Anal. Chem.* **79**, 5117 (2007).
- <sup>29</sup>G. K. Kurup and A. S. Basu, *Biomicrofluidics* **6**, 22008 (2012).
- <sup>30</sup>M. Hein, M. Moskopp, and R. Seemann, *Lab Chip* **15**, 2879 (2015).
- <sup>31</sup>S. Wang, K. J. Sung, X. N. Lin, and M. A. Burns, *PLoS One* **12**, e0173479 (2017).
- <sup>32</sup>S. K. Cho, Y. Zhao, and C.-J. Kim, *Lab Chip* **7**, 490 (2007).
- <sup>33</sup>S. I. Han, H. S. Kim, and A. Han, *Biosens. Bioelectron.* **97**, 41 (2017).
- <sup>34</sup>Y. Wang, Y. Zhao, and S. K. Cho, *J. Micromech. Microeng.* **17**, 2148 (2007).
- <sup>35</sup>H. Lee, L. Xu, and K. W. Oh, *Biomicrofluidics* **8**, 44113 (2014).
- <sup>36</sup>A. Fornell, M. Ohlin, F. Garofalo, J. Nilsson, and M. Tenje, *Biomicrofluidics* **11**, 31101 (2017).
- <sup>37</sup>Z. Ma, D. J. Collins, J. Guo, and Y. Ai, *Anal. Chem.* **88**, 5316 (2016).
- <sup>38</sup>M. Ohlin, A. Fornell, H. Bruus, and M. Tenje, *J. Micromech. Microeng.* **27**, 84002 (2017).
- <sup>39</sup>J. H. Jung, G. Destgeer, B. H. Ha, J. Park, and H. J. Sung, *Lab Chip* **16**, 3253 (2016).
- <sup>40</sup>Y. Bourquin, A. Syed, J. Reboud, L. C. Ranford-Cartwright, M. P. Barrett, and J. M. Cooper, *Angew. Chem., Int. Ed.* **53**, 5587 (2014).
- <sup>41</sup>G. Destgeer, H. Cho, B. H. Ha, J. H. Jung, J. Park, and H. J. Sung, *Lab Chip* **16**, 660 (2015).
- <sup>42</sup>R. J. Shilton, M. Travaglini, F. Beltram, and M. Cecchini, *Adv. Mater.* **26**, 4941 (2014).
- <sup>43</sup>G. Destgeer, S. Im, B. H. Ha, J. H. Jung, M. A. Ansari, and H. J. Sung, *Appl. Phys. Lett.* **104**, 23506 (2014).
- <sup>44</sup>L. V. King, *Proc. R. Soc. London A* **147**, 212 (1934).
- <sup>45</sup>K. Yosioka and Y. Kawasima, *Acta Acust. united Ac* **5**, 167 (1955).
- <sup>46</sup>T. Hasegawa and K. Yosioka, *J. Acoust. Soc. Am.* **46**, 1139 (1969).
- <sup>47</sup>A. A. Doinikov, *Proc. R. Soc. London A* **447**, 447 (1994).
- <sup>48</sup>G. Destgeer, B. H. Ha, J. Park, J. H. Jung, A. Alazzam, and H. J. Sung, *Anal. Chem.* **87**, 4627 (2015).
- <sup>49</sup>J. Lee and K. K. Shung, *J. Acoust. Soc. Am.* **120**, 1084 (2006).
- <sup>50</sup>G. Destgeer, B. H. Ha, J. H. Jung, and H. J. Sung, *Lab Chip* **14**, 4665 (2014).
- <sup>51</sup>J. Wang, J. Wang, L. Feng, and T. Lin, *RSC Adv.* **5**, 104138 (2015).